Latin American Journal of Solids and Structures
www.lajss.org

A Two-Surface Viscoplastic Model for the Structural Steel

Abstract

As extension of the previous two-surface model in plasticity, a two-surface model for viscoplasticity is presented herein. In order to validate and investigate the performance of the proposed model, several numerical simulations are undertaken especially for structural steel under monotonic and cyclic loading cases, where experimental results and numerical results from the rate dependent kinematic hardening model are also provided for the reference. For all the cases studied, the proposed model can appropriately account for the rate-effects in both maximum stress and hysteretic shapes.

Keywords

Two-surface model; Viscoplasticity; Numerical simulation.

Dong-Keon Kim [a]
Jinkyu Kim [b]

[a] Department of Architectural Engineering, Dong-A University, Busan, Korea.
[b] School of Architecture and Architectural Engineering, Hanyang University, Ansan, Kyeonggi-do, Korea, jk295@korea.ac.kr

http://dx.doi.org/10.1590/1679-78253572

Received 02.12.2016
In revised form 16.03.2017
Accepted 10.04.2017
Available online 20.04.2017

1 INTRODUCTION

The general description of material nonlinearity primarily concerns a constitutive equation. Essential ingredients to establish this constitutive equation can be characterized by yield surface (or yield stress function), plastic flow rule, normality rule and hardening law- the yield surface divides the elastic and plastic region; the flow rule relates the plastic strain to stress state; the normality rule leads the incremental plastic strain to the normal level of the yield surface; the hardening law describes the plastic evolution. While the classical rate independent plasticity (so called plasticity) is often illustrated by a single yield surface with either isotropic hardening or kinematic hardening, these models can not completely express the hardening behavior of material. In particular, in the single yield surface model, the elastic domain is considered to be too large compared to experiment results and it is difficult to describe sudden changes from elastic to plastic or plastic to elastic region (Chaboche (2008)). Also, it cannot solely account for cycle-by-cycle accumulation of permanent deformation (ratcheting), which often happen in engineering practice (Bari and Hassan (2008)). In order to account for more realistic response of plasticity, previously, two-surface and multiple yield

surface models have been developed by Mroz (1967), Dafalias and Popov(1975), Krieg (1975), and Banerjee et al. (1987), where key ideas reside in combining the kinematic and the isotropic hardening rules. Among these models, Dargush and Soong (1995) tested the two-surface model by Banerjee et al. (1987) with application to metallic plate dampers, which shows excellent agreement to experimental force-displacement data provided by Tsai et el (1993).

For much elaborate description of material nonlinearity with consideration of strain/stress rate effects under various loading conditions like monotonic, cyclic, and more complex transient dynamic loadings, there have been numerous researches especially for the development of rate-dependent plastic material models and their practical applications in engineering problems. For examples, Bodner and Partom (1972) established a theory of rate-dependent plasticity (or viscoplasticity); Chaboche (1977, 1989) developed a viscoplastic constitutive model with nonlinear kinematic hardening- this model is applied to the 316 stainless steel under cyclic loading and creep relaxation [Chaboche and Rousselier (1983b)]. Later, it is also used for the simulation of ratcheting [Chaboche (1991)]; McDowell (1992) developed viscoplastic nonlinear kinematic hardening model under thermomechanical cyclic conditions, while Tanaka (1994) developed a viscoplastic constitutive model under non-proportional loading; Ohno and Wang (1993) modified Armstrong-Frederick model [Chaboche (1986)] with dynamic recovery term. Tanaka and Yamada (1993), Abdel-Karim and Ohno (2000) continued with this study especially on the nonlinear kinematic hardening model with steady-state ratchetting, while Chaboche-type nonlinear kinematic hardening models for ratchetting are investigated by McDowell (1995), Kang et al. (2001), Kang et al. (2002), Kang el al. (2004), Yaguchi and Takahashi (2000), Yaguchi and Takahashi (2005), and Kang et al. (2006). Main differences in such various viscoplastic models and the classical rate-independent plasticity can be described by overstress and time-dependent behavior. Thus, while elastic strain and strain hardening rules in the viscoplasticity are the same as those in the classical rate-independent plasticity, the stress state goes beyond the elasticity domain whereas this overstress is not allowed in the classical rate-independent plasticity. Also, the viscoplasticity model can describe creep phenomenon (time dependent irreversible deformation for long term response), and it can account for the rate of loading in strain-stress responses, which may become a major issue for earthquake excitation and high velocity impact.

In this paper, we extend the rate independent two-surface model by Banerjee et al. (1987) to the rate dependent two-surface model with consideration of rate-effects. The proposed model is then implemented in commercial finite element software ABAQUS (2008) by using a user subroutine (UMAT), and some representative examples are considered to elucidate the features of the proposed model.

2 A RATE INDEPENDENT TWO-SURFACE PLASTICITY MODEL

In the plasticity, a total strain at a given stress can be decomposed into two parts, which correspond to an elastic strain and plastic strain. For the multiaxial case, this can be generalized as a rate-form as

$$\dot{\varepsilon}_{ij} = \dot{\varepsilon}^{e}_{ij} + \dot{\varepsilon}^{p}_{ij} \tag{1}$$

with the superposed dot indicating a derivative with respect to the time. Thus, $\dot{\varepsilon}^e_{ij}$ and $\dot{\varepsilon}^p_{kl}$ representing the elastic strain rate and the plastic strain rate.

In Eq. (1), the elastic strain rate $\dot{\varepsilon}^e_{ij}$ is related to a stress rate $\dot{\sigma}_{ij}$ with a fourth-order elastic constitutive tensor C^e_{ijkl} as

$$\dot{\sigma}_{ij} = C^e_{ijkl}\dot{\varepsilon}^e_{kl} \tag{2}$$

With Eq. (1), Eq. (2) can be equivalently written as

$$\dot{\sigma}_{ij} = C^e_{ijkl}(\dot{\varepsilon}_{kl} - \dot{\varepsilon}^p_{kl}) \tag{3}$$

As in the classical rate-independent plasticity, the evolution of plastic strain (ε^p_{ij}) and that of yield stress function (or yield surface) are decided by flow rules and hardening laws in the two-surface model. However, this time, there are two yield surfaces, where the kinematic yield surface (or loading surface) in principal stress axes resides inside the isotropic yield surface (or bounding surface) as shown in Figure 1.

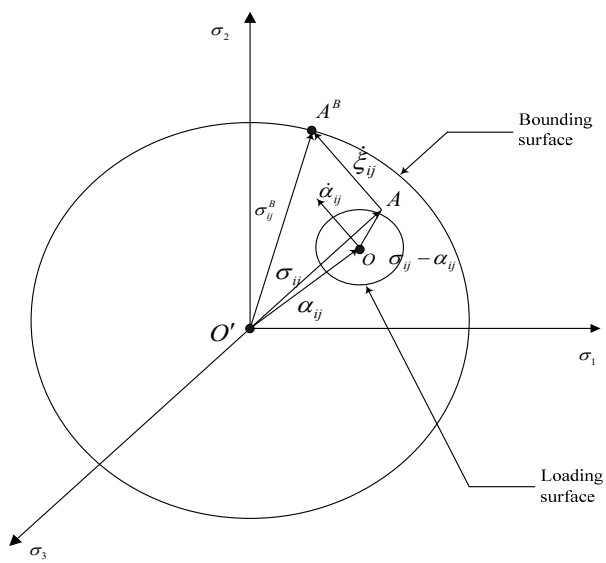

Figure 1: A two-surface model in the rate-independent plasticity.

For the isotropic material, the constitutive relation in this two-surface model of plasticity is identifed as

$$\dot{\sigma}_{ij} = \lambda\delta_{ij}\dot{\varepsilon}_{kk} + 2\mu\dot{\varepsilon}_{ij} \tag{4}$$

in a rate-form of elastic response, where a stress point moves until it reaches the inner yield surface and strains are fully recoverable. Also, when the stress state stays on the inner yielding surface but

resides inside the outer yielding surface (this is usually called transition region or the meta-elastic region), this rate-constitutive relation becomes

$$\dot{\sigma}_{ij} = \lambda\delta_{ij}\dot{\varepsilon}_{kk} + 2\mu\dot{\varepsilon}_{ij} - \frac{3\mu\overline{S}_{ij}\overline{S}_{kl}\dot{\varepsilon}_{kl}}{\left(\sigma_y^L\right)^2\left[1+\frac{H^p}{3\mu}\right]} \tag{5}$$

Further, as the stress state becomes larger, the inner yield surface continuously approaches to the bounding surface and it finally touches the bounding surface and make this bounding surface expand. For this case, the rate-constitutive relation becomes

$$\dot{\sigma}_{ij} = \lambda\delta_{ij}\dot{\varepsilon}_{kk} + 2\mu\dot{\varepsilon}_{ij} - \frac{3\mu S_{ij}S_{kl}\dot{\varepsilon}_{kl}}{\left(\sigma_y^B\right)^2\left[1+\frac{H^p}{3\mu}\right]} \tag{6}$$

In Eqs. (4)-(6), λ is lame's first parameter; μ is shear modulus; σ_y^L is the inner yield stress; σ_y^B is the outer yield stress; S_{ij} is the deviatoric stress; $\overline{S}_{ij}$ is $S_{ij} - \alpha_{ij}$ representing the deviatoric stress minus the back stress; $H^p = h^B\left(\frac{2\sigma_y^B - \xi}{2\sigma_y^B}\right)^{n_1}$ is an isotropic hardening modulus dependent on parameters $\mathrm{h^B}(= \mathrm{h_0^B} + \mathrm{h_1^B}\sigma_y^B)$, h_0^B , h_1^B , n_1 , and $\xi = \sqrt{\xi_{ij}\,\xi_{ij}}$. Here, we only summarize main formulation for the rate-independent two-surface plasticity model. Interested readers can refer to Banerjee et al. (1987), Chopra and Dargush (1994), and Sant (2002).

As described in Figure 1, geometrically, the kinematic hardening of the inner yield surface depends on a vector that joins the stress state to the bounding surface, ξ_{ij} . The location of $\mathrm{A^B}$ is determined by drawing a vector O'$\mathrm{AA^B}$ parallel to OA, σ_{ij}^B . The direction of $\dot{\alpha}_{ij}$is then determined to be paralled to $\mathrm{AA^B}$. The inner surface, which separates the elastic range and inelastic range, is composed of its center and radius expressed by the back stress (α_{ij}) and inner yield stress (σ_y^L). Meanwhile, the outer surface, which always contains the inner yield surface, is located on the center of stress space with a radius represented by the outer yield stress (σ_y^B). The translation of inner surface corresponds to kinematic hardening, while the expansion of outer surface produces isotropic hardening.

3 A RATE DEPENDENT TWO-SURFACE MODEL

3.1 Formulation

Unlike earlier single yield surface models in viscoplasticity that assume all inelastic strain to be rate dependent, in a present two-surface model, the inelastic strain is divided into rate-independent and rate-dependent parts as

$$\dot{\varepsilon}_{ij}^{in} = \dot{\varepsilon}_{ij}^{p} + \dot{\varepsilon}_{ij}^{vp} \tag{7}$$

with $\dot{\varepsilon}_{ij}^{in}$ and $\dot{\varepsilon}_{ij}^{vp}$ representing the inelastic strain-rate and the viscoplastic strain-rate, respectively.

In the past, the above approach had been proven to be effective when accounting for the hysteresis loop with the rounded corners in stress-transition from elastic to inelastic or vice versa [Bradley and Yuen (1983); Tirpitz and Schwesig (1992); Lubliner (2008)]. In addition, as in the existing two-surface plasticity model, a present two-surface viscoplasticity model utilizes the following yield functions such as

$$g_L = \sigma_e - \sigma_y^L = \sqrt{\frac{3}{2}\overline{S}_{ij} : \overline{S}_{ij}} - \sigma_y^L \tag{8}$$

and

$$g_B = \sigma_e - \sigma_y^B = \sqrt{\frac{3}{2}S_{ij} : S_{ij}} - \sigma_y^B \tag{9}$$

depending on kinematic hardening and isotropic hardening rules. Here, σ_e is the von Mises effective stress and the symbol ":" designates the product contracted twice. Thus, three separate regions in Figure 1 are identified with these yield functions: $g_L < 0$ (elasticity); $g_L > 0$ and $g_B < 0$ (meta-elasticity); $g_B > 0$ (both kinematic and isotropic hardening rules are effective). Once the stress-state is identified with these criteria, each portion of the inelastic strain is given by flow rule and nomality hypothesis:

$$\dot{\varepsilon}^{p} = \dot{\lambda}\frac{\partial g_I}{\partial \sigma_{ij}} \quad \text{where } I = B \text{ or } L \tag{10}$$

$$\dot{\varepsilon}^{vp} = \dot{p}\frac{\partial g_I}{\partial \sigma_{ij}} \quad \text{where } I = B \text{ or } L \tag{11}$$

In Eq. (10), the magnitude of the plastic strain increment $\dot{\lambda}$ can be decided by the consistency condition $g_I = \dot{g}_I = 0$. Otherwise, the magnitude of the viscoplastic strain increment $\dot{p}$ is determined from a potential φ

$$\dot{p} = \varphi(\sigma_{ij}, \alpha_{ij}, \sigma_y^B) \tag{12}$$

that is the function of the stress σ_{ij}, the back stress α_{ij}, and the magnitude of bounding surface σ_y^B.

With adoption of the hyperbolic sine function for φ (Dunne and Petrinic, 2005), $\dot{p}$ can be explicitly written as

$$\dot{p} = C\Big[\sinh B(\sigma_e - \sigma_y^B - \sigma_y^L)\Big]^{n_2} = C\left[\sinh B\left(\sqrt{\frac{3}{2}\tilde{S}_{ij} : \tilde{S}_{ij}} - \sigma_y^B - \sigma_y^L\right)\right]^{n_2} \tag{13}$$

In Eq. (13), C and B represent material parameters associated with viscosity. Also, n_2 is a controlling parameter for strain-rate sensitivity [Bodner and Partom (1972), Chaboche (1989)] and $\tilde{S}_{ij}$ represents the deviatoric stress that can be either $\overline{S}_{ij}$ or S_{ij}.

Thus, the viscoplastic strain rate is identified as

$$\dot{\varepsilon}_{ij}^{vp} = \frac{3}{2}\dot{p}\frac{\tilde{S}_{ij}}{\sigma_e} \quad \text{where } \tilde{S}_{ij} = \overline{S}_{ij} \text{ or } S_{ij} \tag{14}$$

and consequently, the inelastic strain is given by

$$\dot{\varepsilon}^{in} = \dot{\lambda}\frac{\partial g_I}{\partial \sigma_{ij}} + \dot{p}\frac{\partial g_I}{\partial \sigma_{ij}} = \frac{C_{ijmn}^e \dfrac{\partial g_I}{\partial \sigma_{mn}} C_{pqkl}^e \dfrac{\partial g_I}{\partial \sigma_{pq}} \dot{\varepsilon}_{kl}}{\dfrac{\partial g_I}{\partial \sigma_{mn}} C_{mnpq}^e \dfrac{\partial g_I}{\partial \sigma_{pq}} - \dfrac{\partial g_I}{\partial \varepsilon_{pq}} \dfrac{\partial g_I}{\partial \sigma_{pq}}} + \frac{3}{2}\dot{p}\frac{\tilde{S}_{ij}}{\sigma_e} \tag{15}$$

Overall, in the present two-surface viscoplasticity model, the consitutive relation of isotropic material results in

$$\dot{\sigma}_{ij} = \lambda\delta_{ij}\dot{\varepsilon}_{kk} + 2\mu\dot{\varepsilon}_{ij} \tag{16}$$

$$\dot{\sigma}_{ij} = \lambda\delta_{ij}\dot{\varepsilon}_{kk} + 2\mu\dot{\varepsilon}_{ij} - \frac{3\mu\overline{S}_{ij}\overline{S}_{kl}\dot{\varepsilon}_{kl}}{\left(\sigma_y^L\right)^2\left[1 + \dfrac{H^p}{3\mu}\right]} - 3\mu\dot{p}\frac{\overline{S}_{ij}}{\sigma_e} \tag{17}$$

$$\dot{\sigma}_{ij} = \lambda\delta_{ij}\dot{\varepsilon}_{kk} + 2\mu\dot{\varepsilon}_{ij} - \frac{3\mu S_{ij}S_{kl}\dot{\varepsilon}_{kl}}{\left(\sigma_y^B\right)^2\left[1 + \dfrac{H^p}{3\mu}\right]} - 3\mu\dot{p}\frac{S_{ij}}{\sigma_e} \tag{18}$$

for the elastic response, kinematic hardening response, and both kinematic and isotropic hardening response, respectively.

3.2 Finite Element Implementation

The present two-surface model for viscoplasticity was implemented by a user subroutine (UMAT) in the ABAQUS (2008). Once the small increment of strain is given, new updated state variables such as stress, back stress, plastic strain, viscoplastic strain are obtained by integrating the constitutive equations. For this numerical simulation, a higher-order adaptive step size Runge-Kutta method is also used to integrate the constitutive equations until a high level of accuracy is obtained. All the equations are expressed by incremental form, which are easily implemented in the Fortran source code. Resulting equations become

$$S_{ij}^{n+1} = S_{ij}^{n} + 2\mu\,\Delta e_{ij}^{n+1} \tag{19}$$

$$\sigma_{ij}^{n+1} = S_{ij}^{n+1} + \frac{1}{3}\delta_{ij}\sigma_{kk}^{n+1} \tag{20}$$

$$\sigma_{ij}^{n} = S_{ij}^{n} + \frac{1}{3}\delta_{ij}\sigma_{kk}^{n} \tag{21}$$

$$e_{ij}^{n} = \varepsilon_{ij}^{n} - \frac{1}{3}\delta_{ij}\varepsilon_{kk}^{n} \tag{22}$$

where e_{ij} is deviatoric strain tensor, and n and $n+1$ represent time-steps.

Subtracting Eq.(21) from Eq.(20) with the strain decomposition, and the relationship between strain and deviatoric strain in Eq.(22), one finds

$$\Delta\sigma_{ij} = 2\mu\left(\Delta\varepsilon_{ij} - \frac{1}{3}\delta_{ij}\Delta\varepsilon_{kk} - \Delta\varepsilon_{ij}^{p} + \frac{1}{3}\delta_{ij}\Delta\varepsilon_{kk}^{p} - \Delta\varepsilon_{ij}^{vp} + \frac{1}{3}\delta_{ij}\Delta\varepsilon_{kk}^{vp}\right) + \frac{1}{3}\delta_{ij}\Delta\sigma_{kk} \tag{23}$$

Using a plastic flow rule and viscoplastic flow rule, Eq.(23) yields

$$\Delta\sigma_{ij} = 2\mu\left(\Delta\varepsilon_{ij} - \frac{1}{3}\delta_{ij}\Delta\varepsilon_{kk} - \dot{\lambda}\frac{\partial g}{\partial\sigma} + \frac{1}{3}\delta_{ij}\dot{\lambda}\frac{\partial g}{\partial\sigma} - \dot{p}\frac{\partial g}{\partial\sigma} + \frac{1}{3}\delta_{ij}\dot{p}\frac{\partial g}{\partial\sigma}\right) + \frac{1}{3}\delta_{ij}\Delta\sigma_{kk} \tag{24}$$

Finally, one can obtain the following incremental formulation.

$$\Delta\sigma_{ij} = 2\mu\Delta\varepsilon_{ij} + \lambda\delta_{ij}\Delta\varepsilon_{kk} - \frac{3\mu S_{ij}S_{kl}\Delta\varepsilon_{kl}}{\left(\sigma_{y}\right)^{2}\left(1+\dfrac{H^{p}}{3\mu}\right)} - 3\mu\Delta p\frac{S_{ij}}{\sigma_{e}} \tag{25}$$

Eq. (25) is numerically into the commercial finite element code, ABAQUS, where a certain iteration scheme is introduced to solve nonlinear equations at the element and global system level (Bathe and Cimento (1980)). The following is a brief explanation about how the nonlinear solver works (here, subscript indices are omitted to avoid complexity). First, all the variables are initialized with corresponding time-step. Then, the solution (${}^{t}U$, nodal displacements) and other internal variables such as strain (${}^{t}\varepsilon$) and stress (${}^{t}\sigma$) are stored at time (t), where the iteration counter (i) is fixed as 1. Variables at the time-step of ($t+\Delta t$) are calculated and updated through iterations with convergence criteria and/or a maximum number of iterations.

For example, the stress is updated from a known converged solution as

$${}^{t+\Delta t}\sigma^{i-1} = {}^{t}\sigma + \int_{t}^{t+\Delta t} {}^{t+\Delta t}C^{i-1}\,d\varepsilon \tag{26}$$

At the element level, the tangent constitutive matrix (${}^{t+\Delta t}C^{i-1}$) is updated with a certain iterative scheme, and consequently, the global stiffness matrix (${}^{t+\Delta t}K^{i-1}$) and nodal force vector (${}^{t+\Delta t}F^{i-1}$) corresponding to the interanl element stresses (${}^{t+\Delta t}\sigma^{i-1}$) are computed by using a gaussian quadrature for each element's integration and collecting them in the following manner.

$$ {}^{t+\Delta t}K^{i-1} = \sum_{e} \int_{V^e} B^T \, {}^{t+\Delta t}C^{i-1} B dV \tag{27} $$

$$ {}^{t+\Delta t}F^{i-1} = \sum_{e} \int_{V^e} B^T \, {}^{t+\Delta t}\sigma^{i-1} dV \tag{28} $$

At the global system level, the solution is obtained in terms of the incremental nodal displacements (ΔU^i) by solving the following set of equations

$$ {}^{t+\Delta t}K^{\,i-1}\Delta U^i = {}^{t+\Delta t}R - {}^{t+\Delta t}F^{i-1} \tag{29} $$

with ${}^{t+\Delta t}R$ representing the externally applied nodal force vector to the time-step, $t+\Delta t$. In solving the global solution of incremental displacement ${}^{i-1}\Delta U^i$, interative scheme is also utilized to update ${}^{t+\Delta t}K^{i-1}$ along with convergence criteria and/or a maximum number of iterations. Finally, the numerical solution of displacements at the time-step ($t+\Delta t$) is updated by

$$ {}^{t+\Delta t}U^i = {}^{t+\Delta t}U^{i-1} + \Delta U^i \tag{30} $$

and strains are calculated from these updated displacements.

In the present work, we adopt the Cash-Karp method (one of embedded Runge-Kutta methods) as the iterative method for updating ${}^{t+\Delta t}C^{i-1}$, while the Newton-Raphson iterative method is used to solve the global system equation with updating ${}^{t+\Delta t}K^{i-1}$.

4 NUMERICAL EXAMPLES

In this section, we verify the present two-surface model for viscoplasticity with representative examples including both monotonic and cyclic loading cases, where both experimental results by Chang (1985) and numerical simulation results by the kinematic hardening model are provided for the reference.

4.1 Experimental Results

For the monotonic loading case, Chang experimentally tests A36 structural steel with three different strain rates of 10^{-3}/sec, 10^{-4}/sec, and 10^{-5}/sec, in each of which loading was increased until 2% axial strain was achieved. Also, in cyclic tests, there are four different types of loading as shown in Figure 2, where all the specimen were loaded in the axial direction and the loading continued until it was stabilized. In particular, for the case 1 and the case 2, the loading was increased until 0.8% axial strain was attained, while the loading was increased until 0.6%, 1.2%, and 1.5% axial strain were obtained for the case 3 and the case 4.

Figure 3-Figure 6 show experimental results of axial stress and axial strain for each loading case, where results from the loading type 3 and the loading type 4 are separately provided for the sake of clarification.

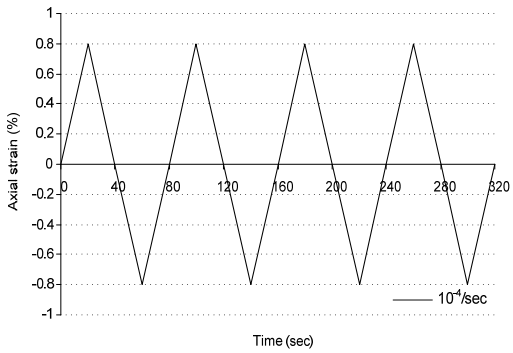

(a) Strain rate of 10^{-4}/sec (Loading Type 1)

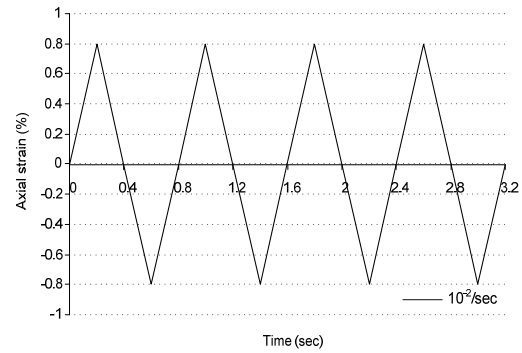

(b) Strain rate of 10^{-2}/sec (Loading Type 2)

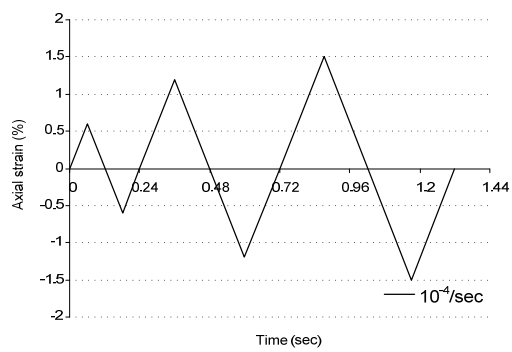

(c) strain rate of 10^{-4}/sec (Loading Type 3)

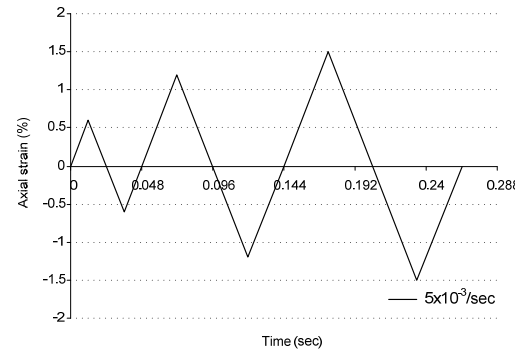

(d) strain rate of 5 x 10^{-3}/sec (Loading Type 4)

Figure 2: Cyclic loading cases.

As shown in Figure 3, three different values of maximum were observed in the monotonic test: 32.5 ksi after initial peak (strain rate 10^{-3}/sec); 30ksi (strain rate: 10^{-4}/sec); 28.5 ksi (strain rate: 10^{-5}/sec). This indicates that the faster strain rate gives the higher stress after yielding. Also, it is observed that the higher strain rate gives the longer plastic plateau and strain hardening effects are negligible in these monotonic tests. With reference to the strain rate of 10^{-5}/sec, the yield stress at a strain rate of 10^{-4}/sec was increased by 5%, and the yield stress at strain rate of 10^{-3}/sec was increased by 14%.

For cyclic tests as shown in Figure 4˜Figure 6, the plastic plateau is no longer observed, however, again, the faster strain rate yields the higher stress. In particular, maximum stresses in the loading type 1 (10^{-4}/sec) and the loading type 2 (10^{-2}/sec) are given by 38.5 ksi and 40.8 ksi, respectively. Also, for the loading type 3 (10^{-4}/sec) and the loading type 4 (strain rate: 5 x 10^{-3}/sec), maximum stresses are identified as: 34 ksi and 37.5 ksi at the 0.6% axial strain; 39 kis and 42.1 ksi at the 1.2% axial strain; 39 ksi and 44.7 ksi at the axial 1.5% strain.

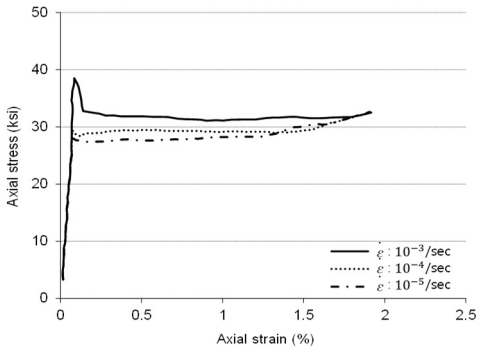

Figure 3: Experimental results under monotonic loading.

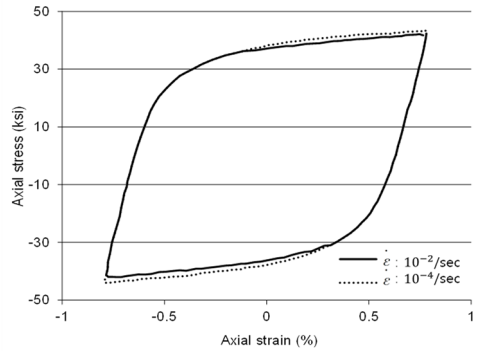

Figure 4: Experimental results under loading type 1 & 2.

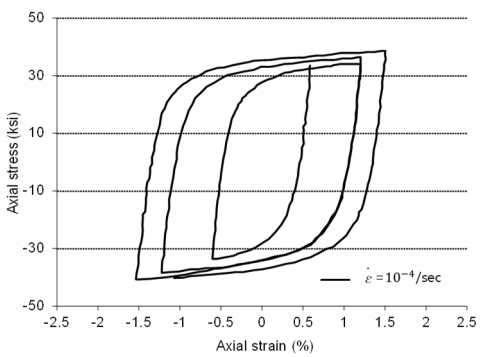

Figure 5: Experimental result under loading type 3.

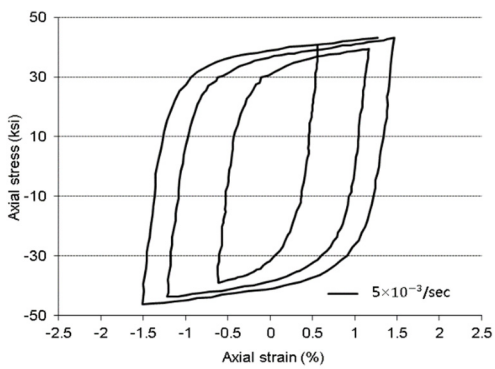

Figure 6: Experimental result under loading type 4.

4.2 Numerical Simulation Results

With a user subroutine (UMAT) in the ABAQUS, both rate-dependent nonlinear kinematic hardening model two-surface models are implemented by the authors. For fair comparison between these two models, we employ one four-node bilinear axisymmetric element (CAX4) for the cylinder-type specimen in every numerical simulation examples, as shown in Figure 7. Also, in numerical simulation, Newton-Raphson method is adopted with fixing the maximum number of iteration as 1000 and incremental displacement as 10^{-9} under such conditions, we checked that all the numerical solutions satisfy convergence criteria of residual force (less than 10^{-5}) and displacement (less than 10^{-8}), respectively.

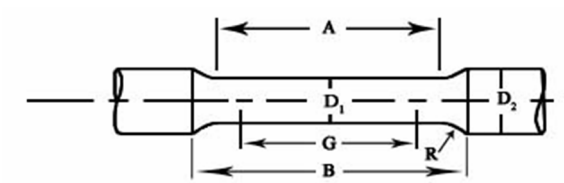

(a) Geometry of specimen

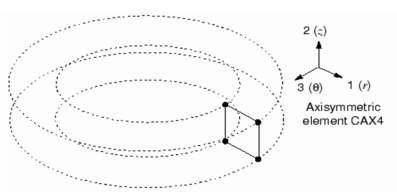

(b) Finite element (CAX4)

Figure 7: Specimens and analytical models.

4.2.1 Nonlinear Kinematic Hardening Model

The main difference between the developed two-surface model and the nonlinear kinematic hardening model [Chaboche, 2008] for the rate-dependent plasticity is that von Mises yield surface cannot expand in the nonlinear kinematic hardening model, while the developed two-surface model allows both expansion and translation of von Mises yield surface. In addition, in the developed two-surface model, we differentiate inelastic strain as the rate-dependent ($\dot{\varepsilon}_{ij}^{vp}$) and the rate-independent part ($\dot{\varepsilon}_{ij}^{p}$) as in Eq. (7). Thus, we have the following equations for the nonlinear kinematic hardening model

$$\dot{\varepsilon}_{ij}^{vp} = \dot{p}\frac{\partial g}{\partial \sigma_{ij}} = \frac{3}{2}\dot{p}\frac{S_{ij}}{\sigma_e} \tag{31}$$

$$\dot{\sigma}_{ij} = C_{ijkl}^{e}(\dot{\varepsilon}_{kl} - \dot{\varepsilon}_{kl}^{vp}) = C_{ijkl}^{e}\left(\dot{\varepsilon}_{kl} - 3\mu\dot{p}\frac{S_{ij}}{\sigma_e}\right) \tag{32}$$

whereas the developed two-surface model has Eqs. (15)-(18).

In numerical simulation of the nonlinear kinematic hardening model, we take material properties and parameters as shown in Table 1.

Young's modulus(E): 28,500 ksi(196,500 MPa), Poisson's ratio (υ) : 0.35
Yield stress(σ_y): 30 ksi (206.84 MPa)
Material parameters of the hyperbolic sine function: C= 1.E+2; B= 1.E-8; n_2 = 5.0

Table 1: Material properties and model parameters employed in the kinematic hardening model.

As shown in Table 1, the yielding stress is specified as 30 ksi (206.84 MPa) for A36 steel, and this value is adopted in numerical simulation with calibration of experimental results from Chang (1985).

Figure 8-Figure 10 show numerical simulation results obtained from the kinematic hardening model. In Figure 8, maximum stress is computed as 32.3 ksi (strain rate 10^{-3}/sec), 30ksi (strain rate: 10^{-4}/sec), and 28.6 ksi (strain rate: 10^{-5}/sec) for the monotonic loading. Also, in cyclic tests, we have maximum stress of 45.6 ksi (loading type 1) and 46.4 ksi (loading type 2). For the other loading types, maximum stresses at each axial strain are obtained as: 33.52 ksi (loading type 4) and 33.51 ksi (loading type 3) at the 0.6% axial strain; 41.8 ksi (loading type 4) and 41.7 ksi (loading type 3) at the 1.2% strain; 46.9 ksi (loading type 4) and 42.2 ksi (loading type 3) at the 1.5% strain.Thus, compared to experimental results, one can check that the nonlinear kinematic hardening model yields reasonably good results in terms of maximum stress for every case. However, this model gives almost linear shape of hysteresis in every stress-strain response that is not well matched to experimental results.

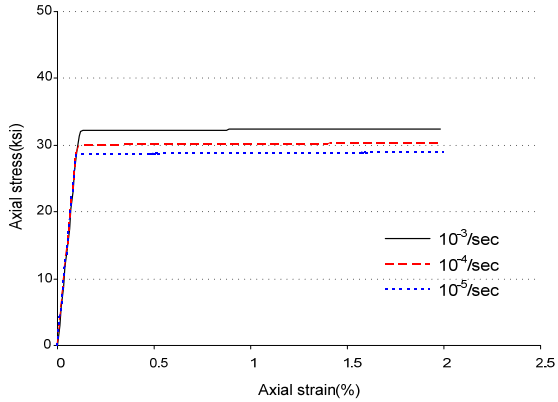

Figure 8: Numerical results under monotonic loading (nonlinear kinematic hardening model).

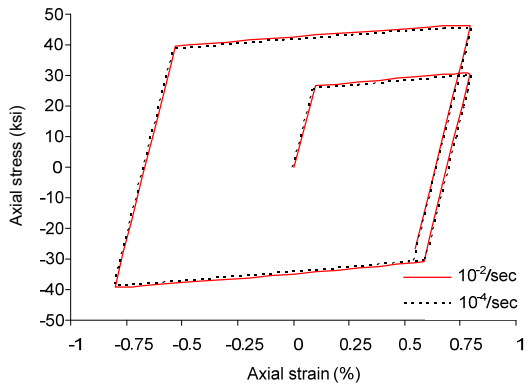

Figure 9: Numerical results under cyclic loadings of type 1 and type 2 (nonlinear kinematic hardening model).

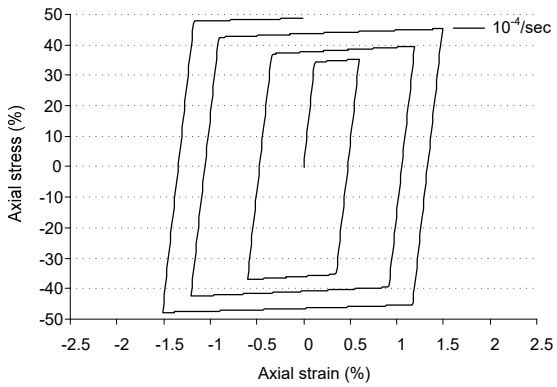

Figure 10: Numerical result under cyclic loadings of type 3 (nonlinear kinematic hardening model).

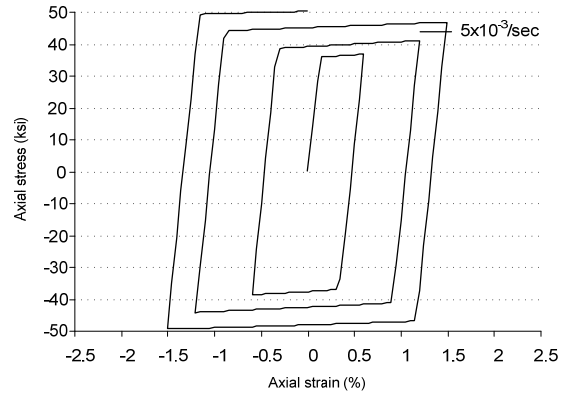

Figure 11: Numerical result under cyclic loadings of type 4 (nonlinear kinematic hardening model).

4.2.2 Two-Surface Model

For numerical simulation of the two-surface model, basically, the same parameters in Table 1 are utilized. Additional parameters adopted in numerical simulation to account for combined effects of both kinematic nd isotropic hardening are summarized in Table 2. In particular, both inner yielding stress and outer yielding stress are introduced here instead of a single yielding stress. Again, every parameter in Table 2 is calibrated from experimental results by Chang (1985), here.

Young's modulus(E): 28,500 ksi(196,500 MPa), Poisson's ratio (υ) : 0.35
Inner yielding stress (σ_y^L) = 30 ksi (206.84 MPa)
Outer yielding stress (σ_y^B) = 60.91 ksi (420MPa)
Hardening parameters: H_0^β = 1650 MPa; h_1^β = -8.47; n_1 = -10.4
Material parameters of the hyperbolic sine function: C = 1.E+2; B= 1.E-8; n_2 = 5.0

Table 2: Additional material properties and model parameters adopted in the two-surface model.

Figure 12-Figure 15 show numerical simulation results obtained from the two-surface model. For the monotonic loading test as shown in Figure 12, numerical results from the two-surface model are exactly the same as those from the rate dependent nonlinear kinematic hardening model. This may indicate that magnitude of the loading and rate of the loading are not large enough to make every response go beyond the outer yielding surface. On the other hand, for cyclic tests, where every response occurs beyond the inner and outer yielding surfaces, the two-surface model is more appropriate than the kinematic hardening model in accounting for both shape of hysteresis and maximum stress values. Thus, for the loading type 1 and the loading type 2, we have maximum stress of MPa (42.5ksi) and Mpa (44.9ksi). Also, for the loading type 3 and the loading type 4, maximum stresses at each axial strain are obtained as: 33.5 ksi (loading type 4) and 37.5 ksi (loading type 3) at the 0.6% axial strain; 41.8 ksi (loading type 4) and 42.1 ksi (loading type 3) at the 1.2% strain; 46.9 ksi (loading type 4) and 44.7 ksi (loading type 3) at the 1.5% strain. All these maximum stresses are much

closer to experimental results, compared to those from the nonlinear kinematic hardening model. Also, for all the cases, the two-surface model gives reasonably good rounded shape of hysteresis as detected in experiments.

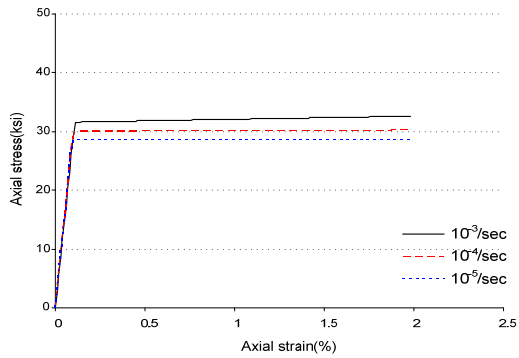

Figure 12: Numerical results under monotonic loading (two-surface model).

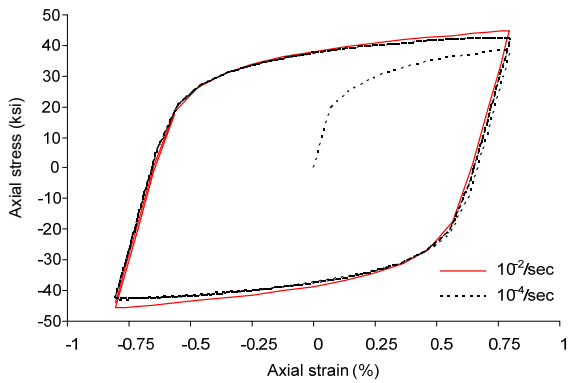

Figure 13: Numerical results under cyclic loadings of type 1 and type 2 (two-surface model).

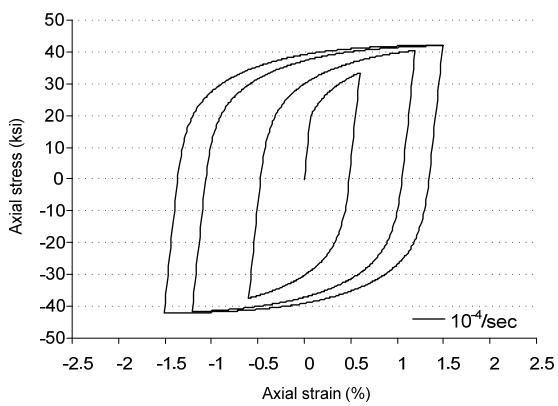

Figure 14: Numerical result under cyclic loadings of type 3 (two-surface model).

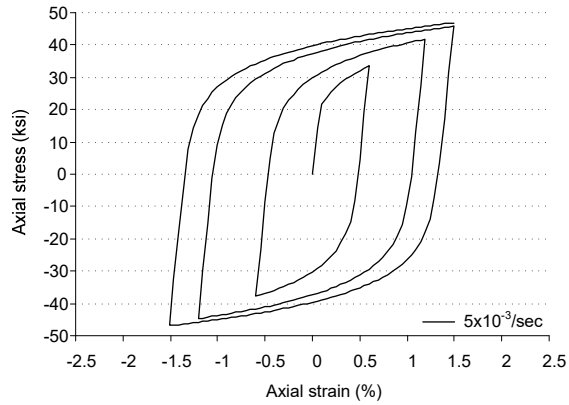

Figure 15: Numerical result under cyclic loadings of type 4 (two-surface model).

5 CONCLUSIONS

In this paper, we develop a two-surface model for rate-dependent plasticity as an extension of the two-surface model in the rate-independent plasticity by Banerjee et al. (1987). The model combines both isotropic and kinematic hardening rules, where the constitutive relation is modified to account for rate-effects. In particular, this model has three separate regions with two bounding surfaces. Thus, when the stress remains in the lower bound, the response is elastic. Also, when stress exceeds the upper bound, the response shows both kinematic and isotropic hardening. In the middle range where the stress resides beteween the lower bound and the upper bound, the response only follows the kinematic hardening rule. With use of a subroutine UMAT, the present model is implemted in the commercial finite element software, ABAQUS. Then, this model is validated through both monotic and cycling loading cases with comparison to experiments and the nonlinear kinematic hardening model. The present model shows excellent agreement with experiments in both maximum stress and shape of hysteresis, while the nonlinear kinematic hardening model is not suitable to account for the shape of hysteresis.

Acknowledgements

This work was supported by the Dong-A University research fund.

References

Abdel-Karim, M.and Ohno, N. (2000). Kinematic hardening model suitable for ratchetting with steady-state. International Journal of Plasticity, 16: 225-240.

Armstrong, P.J. and Frederick, C.O. (1966). A mathematical presentation of the multiaxial Bauschinger effect. CEGB Report RD/B/N731. Berkeley Nuclear Laboratories, Berkeley, UK.

Banerjee, P.K., Wilson, R.B., and Raveendra, S.T. (1987). Advanced applications of BEM to three dimensional problems of monotonic and cyclic plasticity. International Journal of Mechanical Science, 29(9): 637–653.

Bari, S. and Hassan, T. (2000). Anatomy of coupled constitutive models for ratcheting simulation. International Journal of Plasticity, 16: 381–409

Bari, S. and Hassan, T. (2002). An advancement in cyclic plasticity modeling for multiaxial ratchetting simulation. International Journal of Plasticity, 18: 873-894.

Bathe, K. J. and Cimento, A. P. (1980) Some practical procedures for the solution of nonlinear finite element equations. Computer Methods in Applied Mechanics and Engineering, 22: 59-85

Bodner, S.R. and Partom, Y. (1972). A large deformation elastic-viscoplastic analysis of a thick-walled spherical shell. Journal of Applied Mechanics, ASME, 39: 751-757.

Bradley, W.L. and Yuen, S. (1983). A new uncoupled viscoplastic constitutive model. NASA, Lewis Research Center Nonlinear Constitutive Relations for High Temperature Application; 217-234

Chaboche, J.L. (1977). Viscoplastic Constitutive Equations for the Description of Cyclic and Anisotropic Behavior of Metals, Bulletin of Polish Academy of Sciences Technical Sciences, 25: 33-42.

Chaboche. J.L. (1986). Time independent constitutive theories for cyclic plasticity. International Journal of Plasticity, 2: 149-188.

Chaboche. J.L. (1989). Constitutive equations for cyclic plasticity and cyclic viscoplasticity, International Journal of Plasticity, 5: 247-302.

Chaboche. J.L. (1991). On some modifications of kinematic hardening to improve the description of ratcheting effects. International Journal of Plasticity, 7(7): 661–678.

Chaboche. J.L. (2008). A review of some plasticity and viscoplasticity constitutive theories, International Journal of Plasticity, 24: 1642-1693.

Chaboche. J.L., Rousselier. (1983). On the Plastic and Viscoplastic Constitutive Equations-Part II: Application of Internal Variable Concepts to the 316 Stainless Steel. Journal of Pressure Vessel Technology, 105(2): 159-164.

Chang, K.C. (1985). Behaviour of structural steel under cyclic and nonproportional loading. Ph.D dissertation, The State University of New York at Buffalo, USA

Chopra, M.B. and Dargush, G.F. (1994). Development of bem for thermoplasticity. International Journal of Solids and Structures, 31(12/13): 1635-1656

Dafalias, Y.F., Popov, E.P. (1975). A model of nonlinearity hardening materials for complex loading. Acta Mechanica, 21(3): 173–192.

Dargush, G.F. and Soong, T.T. (1995). Behavior of metallic plate dampers in seismic passive energy dissipation systems. Earthquake Spectra, 11(4): 545–568.

Dune, F. and Petrinic, N. (2005) Introduction to computational plasticity, Oxford university press.

Hibbit, Karlsson and Sorensen, Inc. (2008). Abaqus user's guide, v. 6.8. HKS Inc. Pawtucket, RI, USA.

Kalali, A.T, Moud, S.H, and Hassani, B. (2016) Elasto-plastic stress analysis in rotating disks and pressure vessels made of functionally graded materials. Latin American Journal of Solids and Structures, 13(5): 819-834

Kang, G.Z. (2004). A viscoplastic constitutive model for ratchetting of cyclically stable materials and its finite element implementation. Mechanics of Materials, 36:299-312

Kang, G.Z., Gao, Q., and Yang, X.J. (2004). Uniaxial and multiaxial ratchetting of SS304 stainless steel at room temperature: experiments and visco-plastic constitutive model. International Journal of Nonlinear Mechanics, 39: 843-857.

Kang, G.Z., Gao, Q., Cai, L.X., Yang, X.J. Sun, Y.F. (2002). Experimental study on the uniaxial and nonproportionally multiaxial ratchetting of SS304 stainless steel at room and high temperatures. Nuclear Engineering and Design, 216: 13-26.

Kang, G.Z., Gao, Q., Yang, X.J., and Sun, Y.F. (2001). An experimental study on uniaxial and multiaxial strain cyclic characteristics and ratchetting of 316L Stainless Steel, Journal of Materal Science and Technolgy, 18: 219-223.

Kang, G.Z., Kan, Q.H., Zhang, J. (2006). Time-depedent ratcheting experiments of SS304 stainless steel. International Journal of Plasticity, 22: 858-894

Krieg, R.D. (1975). A practical two surface plasticity theory. Journal of Applied Mechanics, ASME, 42(3): 641–646.

Lubliner, Jacob (2008). Plasticity Theory (Revised Edition). Dover Publications.

McDowell, D.L. (1992). A Nonliear Kinematic Hardening Theory for Cyclic Thermoplasticity and Thermoviscoplasticity. International Journal of Plasticity, 8 : 695-728.

McDowell, D.L., (1995). Stress state dependence of cyclic ratchetting behavior of two rail steels. International Journal of Plasticity, 11(4): 397–421.

Mroz, Z., (1967). On the description of anisotropic work hardening. Journal of Mechanics Physics of Solids, 15(3): 163–175.

Ohno, N. and Wang, J.D., (1993a). Kinematic hardening rules with critical state for activation of dynamic recovery, part I, formulation and basic features for ratchetting behavior. International Journal of Plasticity, 9(3): 375–390.

Ohno, N. and Wang, J.D., (1993b). Kinematic hardening rules with critical state for activation of dynamic recovery, part II, application to experiments of ratchetting behavior. International Journal of Plasticity, 9(3): 391–403.

Prager, W. (1956). A new method of analyzing stresses and strains in work hardening plastic solids. Journal of Applied Mechanics, 23: 493-496.

Sant, R.S. (2002). Evolutionary structural optimization for aseismic design. Ph.D dissertation, The State University of New York at Buffalo, USA

Tanaka, E. (1994). A non-proportionality Parameter and a Viscoplastic Constitutive Model Taking into Amplitude Dependencies and Memory Effects of Isotropic Hardening, European Journal of Mechanics A/Solids, 13: 155-173.

Tanaka, E., and Yamada, H. (1993). Cyclic creep, mechanical ratchetting and amplitude history dependence of modified 9Cr–1Mo steel and evaluation of unified constitutive models. Transactions of the Japan Sciety of Mechanical Engineers, 59: 2837–2843.

Tirpitz, E.R. and Schwesig M. (1992) A unified model approach combining rate dependent and rate independent plasticity, Low Cycle Fatigue and Elasto-Plastic Behaviour of Materials, 3: 411-417.

Tsai, K.C., Chen, H.W., Hong, C.P., Su, Y.F. (1993). Design of steel triangular plate energy absorbers for seismic resistant construction. Earthquake Spectra, 9(3): 505–528.

Yaguchi, M., Takahashi, Y., (2000). A viscoplastic constitutive model incorporating dynamic strain aging effect during cyclic deformation conditions. International Journal of Plasticity, 16: 241–262.

Yaguchi, M., Takahashi, Y., (2005b). Ratchetting of viscoplastic material with cyclic softening. Part 2. Application of constitutive models. . International Journal of Plasticity, 21: 835-860.